JOURNAL OF GEOPHYSICAL RESEARCH, VOL. 115, D00H16, doi:10.1029/2009JD012251, 2010

Click Here for Full Article

The GCM-Oriented CALIPSO Cloud Product (CALIPSO-GOCCP)

H. Chepfer,[1] S. Bony,[1] D. Winker,[2] G. Cesana,[3] J. L. Dufresne,[1] P. Minnis,[2] C. J. Stubenrauch,[3] and S. Zeng[4]

Received 14 April 2009; revised 17 September 2009; accepted 13 October 2009; published 4 March 2010.

[1] This article presents the GCM-Oriented Cloud-Aerosol Lidar and Infrared Pathfinder Satellite Observation (CALIPSO) Cloud Product (GOCCP) designed to evaluate the cloudiness simulated by general circulation models (GCMs). For this purpose, Cloud-Aerosol Lidar with Orthogonal Polarization L1 data are processed following the same steps as in a lidar simulator used to diagnose the model cloud cover that CALIPSO would observe from space if the satellite was flying above an atmosphere similar to that predicted by the GCM. Instantaneous profiles of the lidar scattering ratio (SR) are first computed at the highest horizontal resolution of the data but at the vertical resolution typical of current GCMs, and then cloud diagnostics are inferred from these profiles: vertical distribution of cloud fraction, horizontal distribution of low, middle, high, and total cloud fractions, instantaneous SR profiles, and SR histograms as a function of height. Results are presented for different seasons (January–March 2007–2008 and June–August 2006–2008), and their sensitivity to parameters of the lidar simulator is investigated. It is shown that the choice of the vertical resolution and of the SR threshold value used for cloud detection can modify the cloud fraction by up to 0.20, particularly in the shallow cumulus regions. The tropical marine low-level cloud fraction is larger during nighttime (by up to 0.15) than during daytime. The histograms of SR characterize the cloud types encountered in different regions. The GOCCP high-level cloud amount is similar to that from the TIROS Operational Vertical Sounder (TOVS) and the Atmospheric Infrared Sounder (AIRS). The low-level and middle-level cloud fractions are larger than those derived from passive remote sensing (International Satellite Cloud Climatology Project, Moderate-Resolution Imaging Spectroradiometer–Cloud and Earth Radiant Energy System Polarization and Directionality of Earth Reflectances, TOVS Path B, AIRS–Laboratoire de Météorologie Dynamique) because the latter only provide information on the uppermost cloud layer.

Citation: Chepfer, H., S. Bony, D. Winker, G. Cesana, J. L. Dufresne, P. Minnis, C. J. Stubenrauch, and S. Zeng (2010), The GCM-Oriented CALIPSO Cloud Product (CALIPSO-GOCCP), *J. Geophys. Res.*, *115*, D00H16, doi:10.1029/2009JD012251.

1. Introduction

[2] The definition of clouds or cloud types is not unique. It differs among observations (e.g., clouds detected by a lidar may not be detected by a radar or by passive remote sensing), and between models and observations (e.g., models predict clouds at each atmospheric level where condensation occurs, while observations may not detect clouds overlapped by thick upper-level clouds). A comparison between modeled and observed clouds thus requires a consistent definition of clouds, taking into account the effects of viewing geometry, sensors' sensitivity and vertical overlap of cloud layers. For this purpose, clouds simulated by climate models are often compared to observations through a model-to-satellite approach: model outputs are used to diagnose some quantities that would be observed from space if satellites were flying above an atmosphere similar to that predicted by the model [e.g., *Yu et al.*, 1996; *Stubenrauch et al.*, 1997; *Klein and Jakob*, 1999; *Webb et al.*, 2001; *Zhang et al.*, 2005; *Bodas-Salcedo et al.*, 2008; *Chepfer et al.*, 2008; *Marchand et al.*, 2009].

[3] Within the framework of the Cloud Feedback Model Intercomparison Program (CFMIP) (see http://www.cfmip.net), a package named the CFMIP Observation Simulator Package (COSP) has been developed to compare in a consistent way the cloud cover predicted by climate models with that derived from different satellite observations. This package includes in particular an International Satellite Cloud Climatology Project (ISCCP) simulator [*Klein and Jakob*, 1999; *Webb et al.*, 2001], a CloudSat simulator [*Haynes et al.*, 2007], and a Cloud-Aerosol Lidar and Infrared Pathfinder Satellite Observation (CALIPSO)

[1]Laboratoire de Météorologie Dynamique, IPSL, Université Paris 6, Centre National de la Recherche Scientifique, Paris, France.
[2]NASA Langley Research Center, Hampton, Virginia, USA.
[3]Laboratoire de Météorologie Dynamique, IPSL, Ecole Polytechnique, Centre National de la Recherche Scientifique, Palaiseau, France.
[4]LOA, UFR de Physique, Université des Sciences et Technologies de Lille, Villeneuve d'Ascq, France.

Copyright 2010 by the American Geophysical Union.
0148-0227/10/2009JD012251$09.00

simulator [*Chepfer et al.*, 2008]. Additionally, it includes a Subgrid Cloud Overlap Profile Sampler Subgrid Cloud Overlap Profile Sampler [*Klein and Jakob*, 1999] that divides each model grid box into an ensemble of subcolumns generated stochastically and, in which the cloud fraction is assigned to be 0 or 1 at every model level, with the constraint that the cloud condensate and cloud fraction averaged over all subcolumns is consistent with the grid-averaged model diagnostics and the cloud overlap assumption.

[4] The purpose of this article is to present a data set, named the GCM-Oriented CALIPSO Cloud Product (GOCCP), that diagnoses cloud properties from CALIPSO observations exactly in the same way as in the simulator (similar spatial resolution, same criteria used for cloud detection, same statistical cloud diagnostics). This ensures that discrepancies between model and observations reveal biases in the model's cloudiness rather than differences in the definition of clouds or of diagnostics.

[5] Section 2 describes the processing of CALIPSO Cloud-Aerosol Lidar with Orthogonal Polarization (CALIOP) Level 1 data [*Winker et al.*, 2007] leading to the GOCCP data set, and presents globally averaged results for June, July, and August (JJA) 2006–2007–2008 and January, February, and March (JFM) 2007–2008. The sensitivity of observed cloud diagnostics to the vertical resolution and to the cloud detection threshold is evaluated in section 3. Day/night variabilities of cloud characteristics are discussed in section 4, together with an illustration of GOCCP results along the Global Energy and Water Cycle Experiment (GEWEX) Pacific Cross-Section Intercomparison Transect (GPCI) (see http://gcss-dime.giss.nasa.gov/gpci/modsim_gpci_models.html). GOCCP results are then compared with other cloud climatologies in section 5, and conclusions are drawn in section 6.

2. Processing of CALIOP Level 1 Data

2.1. Calculation of the Scattering Ratio

[6] Here we use the Attenuated Backscattered profile at 532 nm (ATB, collection V2. 01) that is part of the CALIOP lidar Level 1 data set. CALIOP is aboard CALIPSO, a nearly Sun-synchronous platform that crosses the equator at about 0130 LST [*Winker et al.*, 2007, 2009]. The original ATB horizontal resolution is 330 m below 8 km of altitude and 1 km above. The original ATB vertical resolution is 30 m below 8 km of altitude and 60 m above; total of 583 vertical levels are distributed from the surface up to 40 km. The Molecular Density profile (MD) is derived from Goddard Modeling and Assimilation Office (GMAO) atmospheric profiles [*Bey et al.*, 2001] for 33 vertical levels.

[7] In the COSP software, both the CALIPSO and the CloudSat simulator results are computed on a vertical grid of 40 equidistant levels (height interval, Δz = 480 m) distributed from the sea level to 19 km. The ATB profile (583 vertical levels, Figure 1a) and the MD profile (33 vertical levels) are each independently averaged or interpolated onto the 40-level vertical grid, leading to the ATB_{vert} and MD_{vert} profiles. This averaging significantly increases the ATB signal-to-noise ratio.

[8] To convert the MD profile into molecular ATB, ATB_{vert} and MD_{vert} profiles are analyzed and averaged in cloud-free portions of the stratosphere: $22 < z < 25$ km for nighttime data ($20 < z < 25$ km for daytime), and $28.5 < z < 35$ km in the Southern Hemisphere (60°S–90°S) during winter (June–October) to avoid Polar Stratospheric Clouds. At these altitudes z, ATB_{vert} and MD_{vert} profiles are each averaged horizontally over ±33 profiles (±10 km) on both sides of a given profile.

[9] The ratio between these two values ($R = \langle ATB_{vert} \rangle / \langle MD_{vert} \rangle$) in the cloud-free stratosphere is then used to scale the MD_{vert} profile into an Attenuated Backscatter Molecular signal profile ($ATB_{vert,mol}$). This latter represents the ATB profile that would be measured in the absence of clouds and aerosols in the atmosphere. The lidar scattering ratio (SR) vertical profile is then computed by dividing the ATB_{vert} profile by the $ATB_{vert,mol}$ profile. Its horizontal resolution is 330 m and the vertical resolution (40 levels) is close to that of GCMs (Figures 1b, 1d, 2b, and 2d).

[10] Despite the vertical averaging, the signal-to-noise ratio remains low during daytime in clear-sky regions because of the large number of solar photons reaching the lidar's telescope (Figures 2b and 2d). However, the laser light reflection on optically thick clouds decreases the signal-to-noise ratio in the stratosphere, giving anomalous R values. Therefore, daytime profiles with R values significantly different from those associated with nighttime profiles ($R > 0.95$ or $R < 0.14$) are rejected. They represent about 30% of the total number of level 1 V2.01 daytime profiles (e.g., Figure 2c). Pixels located below and at the surface level are rejected by using the "altitude elevation" flag from level 1 CALIOP data.

2.2. Definition of Cloud Diagnostics

[11] Here we present how cloud detection is performed for each lidar profile, and then how monthly statistical summaries are produced.

2.2.1. Cloud Detection on a Single Profile

[12] Several simple diagnostics are derived from the SR profile. Different SR thresholds are used to label each atmospheric layer (Figures 1d and 2d) as cloudy (SR > 5), clear (0.01 < SR < 1.2), fully attenuated (SR < 0.01), or unclassified (1.2 < SR < 5 or $ATB - ATB_{mol} < 2.5.10^{-3}$ km^{-1} sr^{-1}) to avoid false cloud detection in the upper troposphere/lower stratosphere, where the ATB_{mol} is very low. We then determine if the profile contains at least one cloud layer within the low-level ($P > 680$ hPa), middle-level ($440 < P < 680$ hPa) and highest-level ($P < 440$ hPa) atmospheric layers, and in the whole column. To keep detailed information about the distribution of the lidar signal intensity, we also record the occurrence frequency of different SR values (we use 15 intervals of SR values, ranging from 0 to 100) as a function of height (y axis) to built the histograms of SR values (referred to as SR CFAD532 in the GOCCP data set).

2.2.2. Monthly Cloud Diagnostics

[13] Monthly cloud fractions are then computed at each vertical level (or at low-, middle-, and highest-level layers) by dividing, for each longitude-latitude grid box (e.g., 1° × 1° or 2.5° × 2.5°), the number of cloudy profiles encountered during one month by the total number of instantaneous SR profiles (not fully attenuated) measured during that month. In the GOCCP database, cloud layer diagnostics are referred to as "low, middle, and high layered cloud

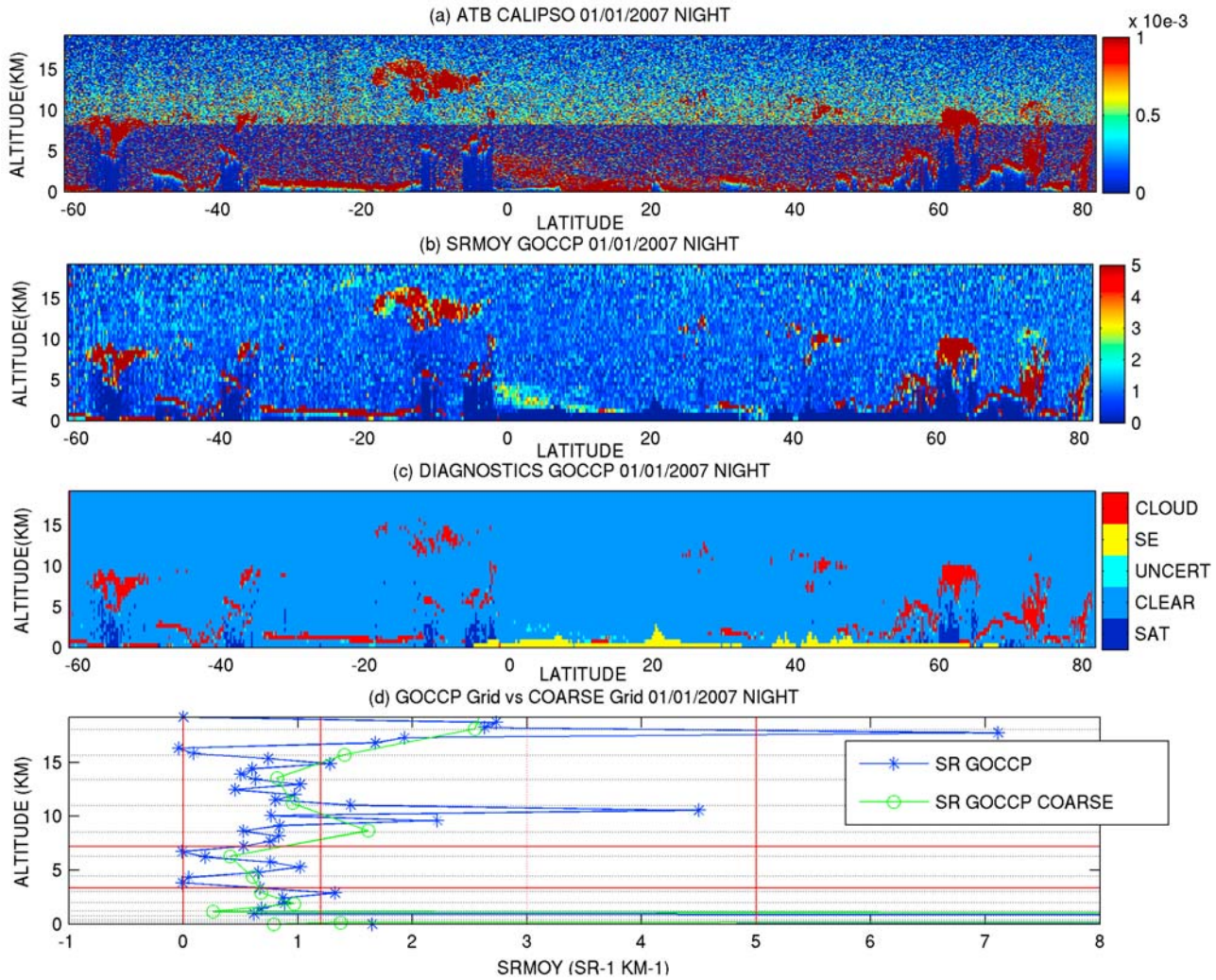

Figure 1. One orbit. (a) Attenuated backscattered (ATB) signal, Cloud-Aerosol Lidar with Orthogonal Polarization level 1 product, 583 vertical levels. (b) Lidar scattering ratio (SR) over the 40 vertical equidistant levels grid. (c) GCM-Oriented Cloud-Aerosol Lidar and Infrared Pathfinder Satellite Observation Cloud Product (GOCCP) diagnostics: cloudy, clear, uncertain, fully attenuated (SAT), below the surface level (SE). (d) Example of one single vertical profile of the scattering ratio for the standard 40-level grid and the coarse 19-level grid: vertical bars correspond to the diagnostic thresholds (SR = 5, SR = 1.2, SR = 0.01). The red horizontal lines show the limits of the low, middle, and high atmospheric layers.

fractions'' and monthly mean three-dimensional distributions of the cloud fraction as ''3-D cloud fraction.''

[14] Monthly SR histograms (which provide information about the variability of the SR signal) are also computed by accumulating the instantaneous SR histograms over a month in each grid box and each vertical layer. Each of these diagnostics has its counterpart included in the lidar simulator outputs of COSP.

2.3. June–August and January–March Results

[15] In this section we present the seasonal mean results for JJA and JFM obtained for the 40 levels vertical grid and for a horizontal resolution of 2.5° (latitude) × 3.75° (longitude).

2.3.1. Maps of Total and Layered Cloud Fractions

[16] As shown by Table 1, the total cloud cover is larger over ocean (0.71) than over land (0.57), with a global average of 0.66. This is lower than the global cloud cover of 76% determined by *Mace et al.* [2009], using a combined CALIPSO-CloudSat product. The latter corresponds to the cloud cover of CALIOP-NASA L2, since CALIOP is sensitive to thinner clouds than CloudSat. For high clouds the horizontal averaging can be up to 80 km to detect subvisible cirrus, whereas CALIOP-GOCCP applies vertical averaging which is not sensitive to the detection of very thin cirrus. The analysis of *Sassen and Wang* [2008] using CloudSat data alone, leads to a cloud cover of 64.0% over ocean and of 54.7% over land, whereas CALIOP-NASA L2 yields 84% and 63%, respectively. As expected, Figure 3a shows that the minimum total cloud cover occurs over subtropical deserts (Sahara, South Africa, Australia, etc), and the maxima are found over the Intertropical Convergence Zone (ITCZ), in midlatitudes storm tracks, and at the

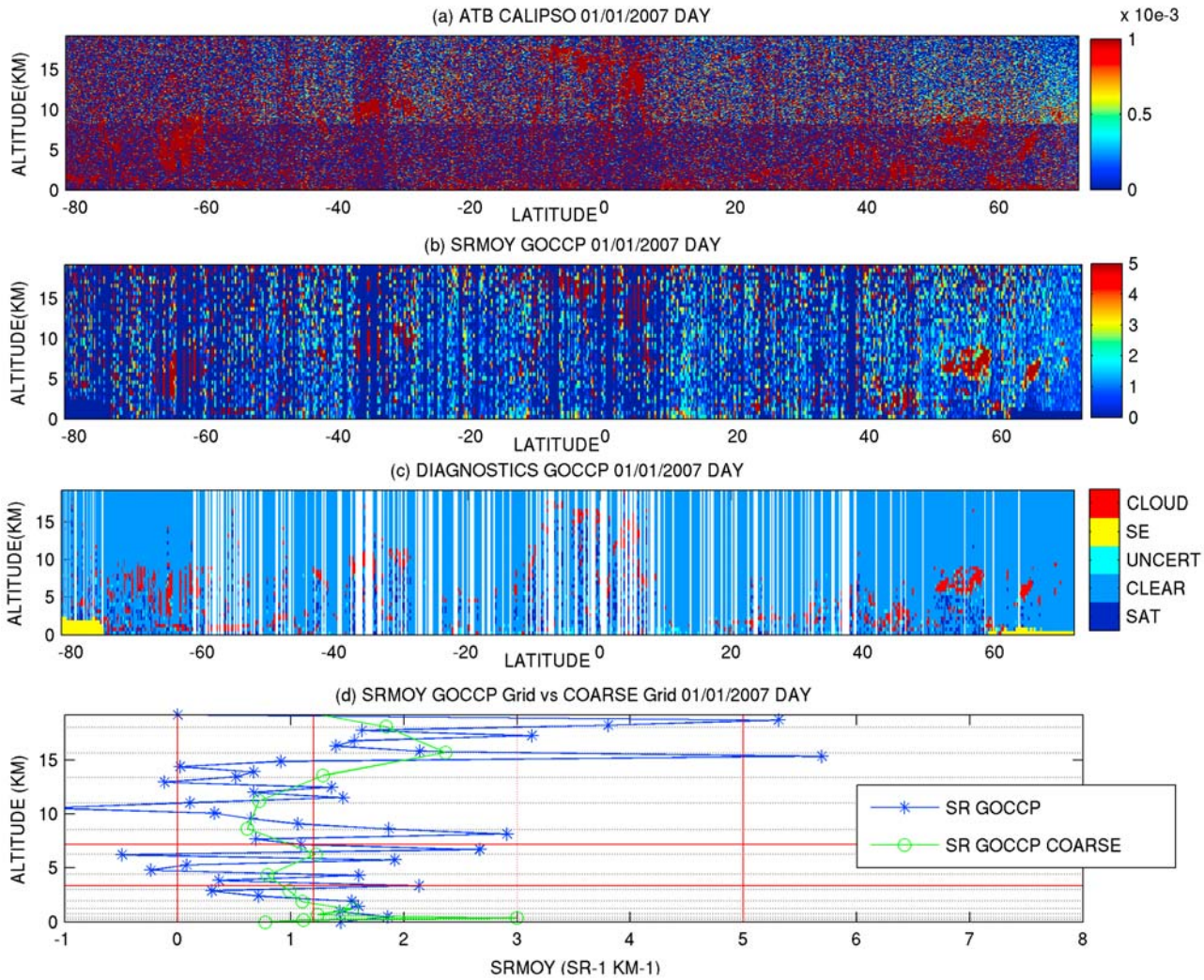

Figure 2. Same as Figure 1, but for one daytime orbit. In Figure 2c, the white lines correspond to regions where the profiles have been rejected because the noise was too large (see text).

eastern sides of the ocean basins associated with persistent low-level stratiform cloudiness (Figure 3a). Maps of low-level, middle-level, and highest-level cloud fractions (Figures 3b–3h) show the predominance of low-level clouds over the oceans, both in the tropics and in the extratropics, and a striking land-sea contrast in the low-level cloud fraction. Low-level cloud fractions of about 0.3–0.4 are found in the trade wind areas (typically covered by shallow cumulus clouds), while amounts exceeding 0.6 occur in the midlatitudes. Small low-level cloud fractions are reported only in the deep convective regions (warm pools, ITCZ), where thick high-level clouds attenuate the lidar signal so much that low-level clouds cannot be detected.

[17] At the global scale, the change in total cloud amount is less than 0.01 between JJA and JFM (Table 1). This is in agreement with other observations: when considering the whole globe, cloud fraction does not change with season; only its distribution changes. ISCCP and TOVS Path-B report 0.65/0.70 in JJA and 0.67/0.72 in JFM, respectively. The main seasonal cloud fraction variation (Figures 3e–3h for JJA versus Figures 3a–3d for JFM) occurs in tropical regions (between 30°N and 20°S), where both oceanic and land cloud cover changes follow the seasonal latitudinal migration of the ITCZ. The middle and high cloud cover seasonal variations are similar (Figure 3) because the middle-level clouds are often associated with high clouds. The largest seasonal variation for both cloud layers is associated with deep convection over continents.

2.3.2. Vertical Distribution of Clouds

[18] The zonally averaged vertical distribution of the GOCCP cloud fraction, together with the fractional area of each grid box (or each latitude) associated with clear-sky or undefined situations, are shown in Figure 4. At each altitude, the sum of cloudy, clear, undefined areas is equal to 1. The zonal mean cloud fraction is maximal within the atmospheric boundary layer (below 3 km), except at very low latitudes where highest-level clouds mask lower-level clouds (as indicated by the maximum of the fully attenuated fraction). The midlatitude cloudiness occurs at all levels of the atmosphere, with a maximum at low levels. Such a structure is expected in regions where baroclinic instabilities produce frontal clouds over the whole depth of the troposphere and where anticyclonic situations produce boundary layer clouds. Equatorward of about 10° of latitude, the cloud fraction is greatest at heights between 12 and 14 km. In the

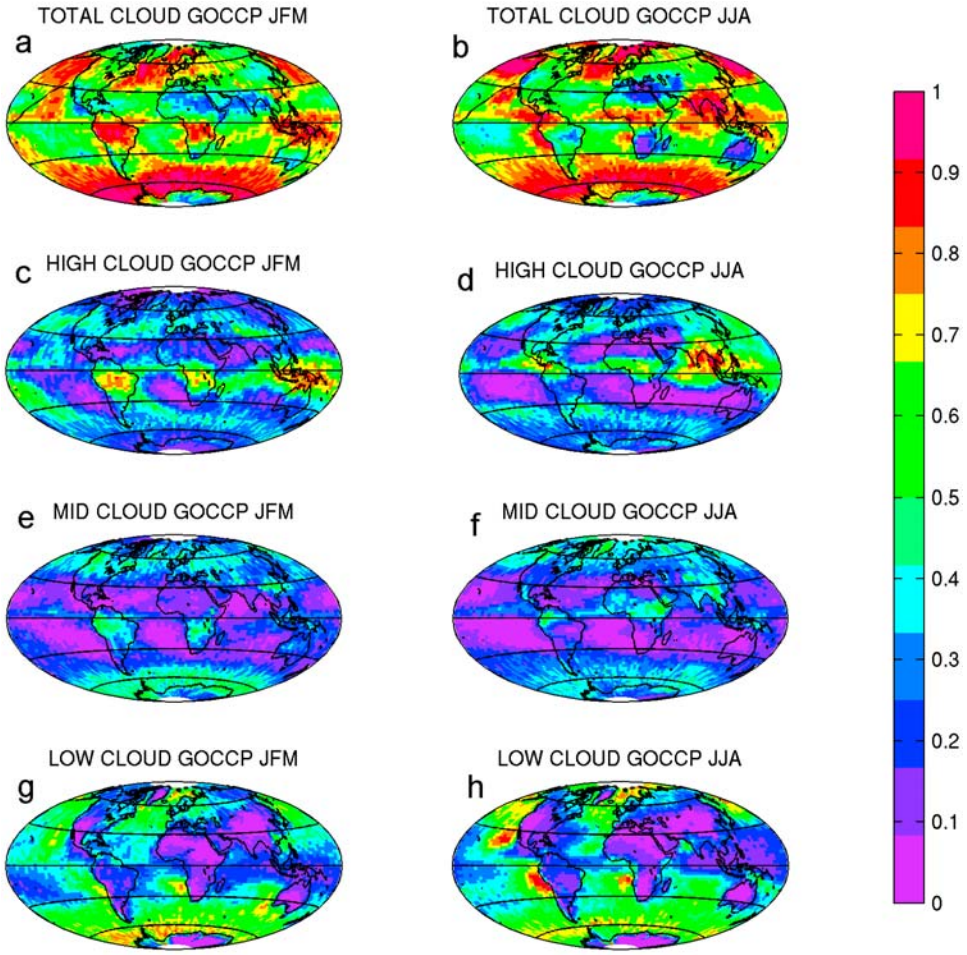

Figure 3. GOCCP (a–b) total, (c–d) highest-level, (e–f) middle-level, and (g–h) low-level cloud fraction (averaged over day and night) for (left) January, February, and March (JFM) and (right) June, July, and August (JJA).

tropics, this atmospheric layer corresponds to the layer where extensive anvil clouds are formed by the detrainment of hydrometeors from convective systems [e.g., *Folkins et al.*, 2000]. The features of Figure 4 agree roughly with *Mace et al.* [2009, Figure 8], but the absolute values, especially for high clouds, are lower, again because of the different detection thresholds of thin cirrus by CALIOP-NASA and CALIOP-GOCCP.

[19] The uncertain situations (Figure 4d) correspond to cases in which the SR signal is too high for a clear-sky situation, but is too low to unambiguously define the presence of a cloud layer. These situations may occur where boundary layer aerosols are abundant (e.g., over the Atlantic windward of the Sahara), or where the cloudiness is too thin or too broken to pass the cloud detection threshold (SR = 5).

2.3.3. SR Histograms

[20] Histograms of SR provide a summary of the occurrence of the different SR values encountered within a grid box at a given altitude. Each histogram is normalized by dividing the occurrence in each SR altitude box by the total number of occurrences in the histogram. This diagnostic is the lidar counterpart of the joint height-reflectivity histogram derived from Cloudsat radar data for comparable vertical grids [e.g., *Zhang et al.*, 2007; *Bodas-Salcedo et al.*, 2008; *Marchand et al.*, 2009].

Table 1. Cloud Fraction From Standard GOCCP for Two Seasons[a]

	Night		Day	
GOCCP	JFM	JJA	JFM	JJA
		Global		
Total	0.66	0.66	0.66	0.66
Low	0.36	0.36	0.36	0.37
Middle	0.20	0.19	0.27	0.25
High	0.29	0.29	0.35	0.33
		Land		
Total	0.55	0.54	0.61	0.61
Low	0.20	0.15	0.26	0.25
Middle	0.26	0.24	0.32	0.31
High	0.28	0.31	0.34	0.34
		Ocean		
Total	0.71	0.71	0.68	0.68
Low	0.44	0.45	0.41	0.42
Middle	0.18	0.17	0.24	0.23
High	0.29	0.28	0.35	0.33

[a]Detection threshold SR = 5 and COSP vertical grid of 40 equidistant vertical levels. Abbreviations are as follows: JFM, January, February, and March; JJA, June, July, and August.

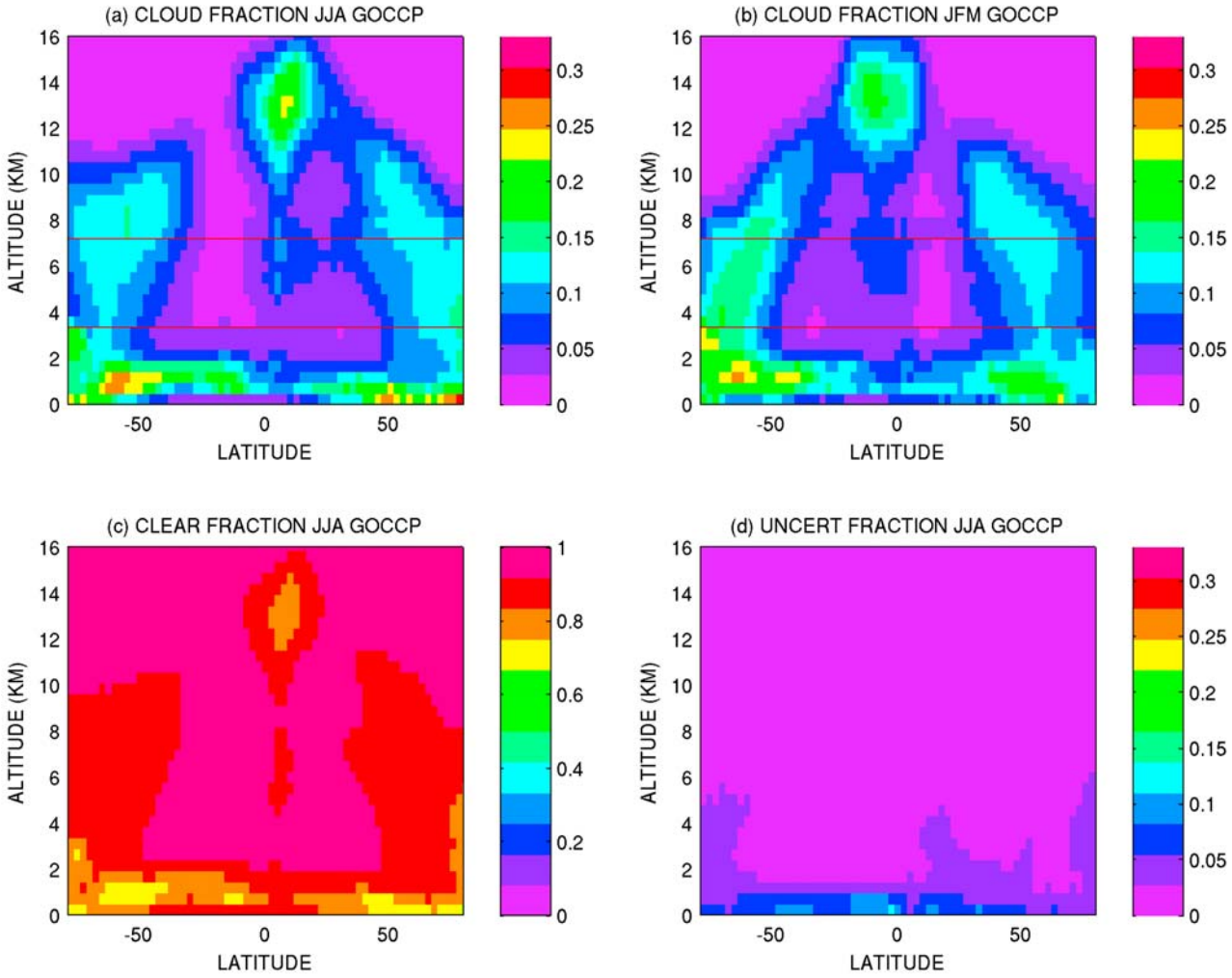

Figure 4. Vertical distributions of the GOCCP cloud fraction for JJA and JFM (GOCCP-SR5). Zonally averaged fractions of the longitude-latitude grid boxes flagged as cloudy for (a) JJA and (b) JFM, (c) clear JJA, and (d) uncertain JJA. In each longitude-latitude grid box and each atmospheric layer, the sum of the fractions from Figures 4a, 4c, and 4d equals 1. The red horizontal lines show the limits of the low, middle, and high atmospheric layers used to define the layered cloud fractions.

[21] Figure 5 shows histograms of SR aggregated for various regions and for two seasons (JFM and JJA). Those exhibit different patterns depending on the prominent cloud types in presence. Over the tropical western Pacific warm pool, deep convective cloud systems produce many large SR values (>10) at altitudes between 12 and 15 km (Figure 5a) and numerous cases of fully attenuated values (SR < 0.01) below 8 km (related to the attenuation of the low-altitude lidar signal by the overlapping thick cloud layers). Secondary maxima in the SR histogram also appear in the mid-troposphere (5–9 km), which is consistent with the large abundance of thick congestus clouds over this region [*Johnson et al.*, 1999], and at low levels (below 3 km) associated with the presence of small shallow cumulus clouds. On the contrary, the SR histogram associated with California stratocumulus clouds exhibits two distinctive maxima: the first one below 3 km, where numerous low-level clouds produce a wide range of SR values between 3 and 80, and the second one around 10 km associated with the presence of thin cirrus clouds. Note that values of 3 < SR < 5 above 14 km are due to observational noise and thus have no geophysical meaning; they do not pass the test, $ATB\text{-}ATB_{mol} < 2.5.10^{-3}$ km^{-1} sr^{-1} (defined in section 2.2). In the midlatitude North Pacific region, the SR histogram exhibits a large range of SR values over the whole troposphere and a substantial number of fully attenuated values below 5 km, consistent with the presence of thick, high-topped frontal clouds of large vertical extent in regimes of synoptic ascent (e.g., baroclinic fronts) and the presence of low-level clouds in regimes of synoptic descent [e.g., *Lau and Crane*, 1995; *Norris and Iacobellis*, 2005].

3. Sensitivity to Horizontal Sampling, Vertical Averaging, and Cloud Detection Thresholds

3.1. Sensitivity to Horizontal Sampling

[22] All the GOCCP cloud diagnostics are derived at the full horizontal resolution of CALIOP Level 1 data (330 m along the track below 8 km and 1 km above 8 km). They are based on a procedure that, at this resolution, declares each atmospheric layer as totally "clear," "undefined," "fully

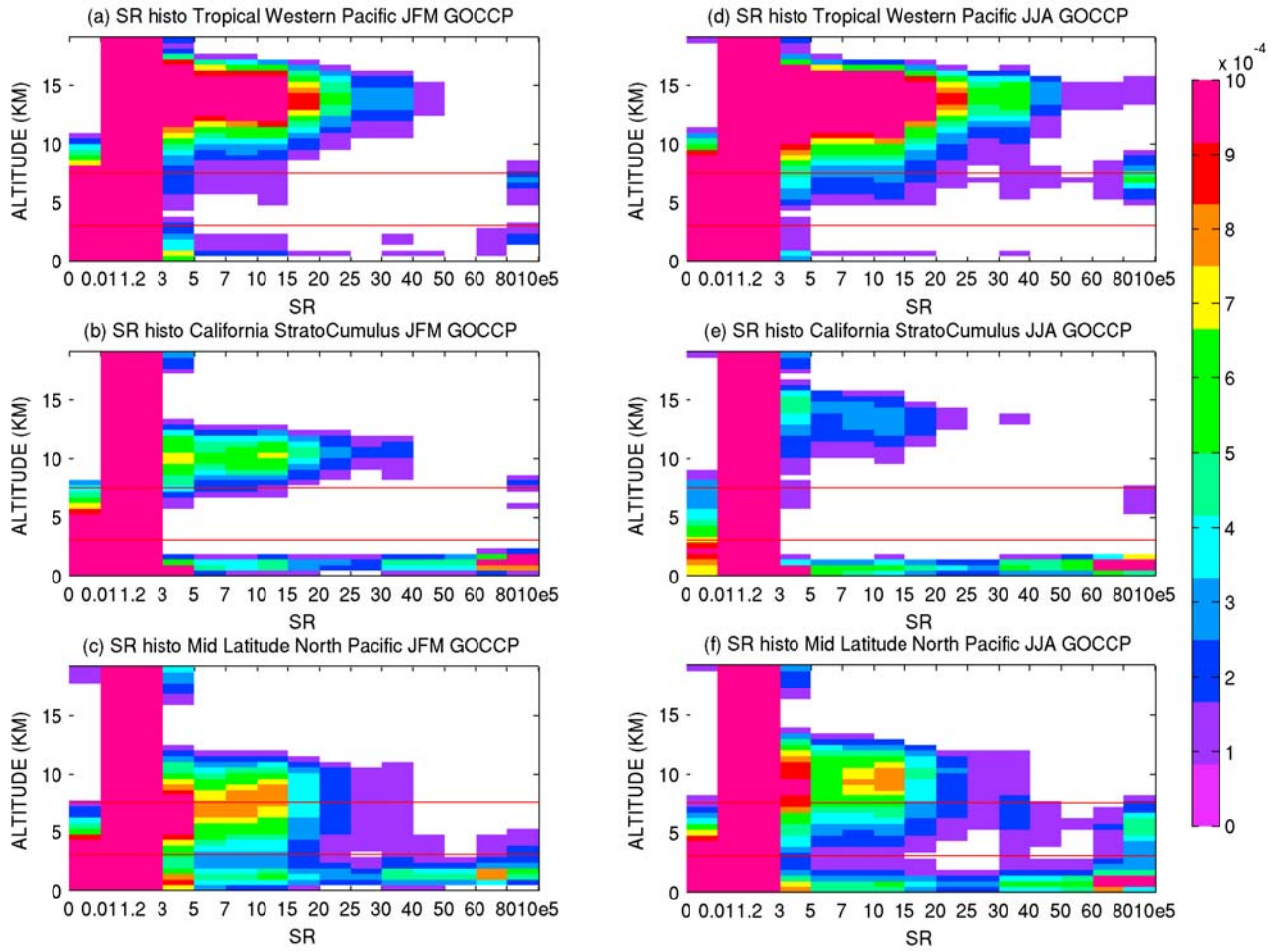

Figure 5. Joint height-SR histogram for (left) JFM and (right) JJA derived from GOCCP nighttime data for three different regions: (a and d) tropical western Pacific (5°S–20°N, 70°E–150°E), (b and e) California stratus region (15°N–35°N, 110°W–140°W), and (c and f) North Pacific (30°N–60°N, 160°E–140°W). In each plot, the vertical axis is the altitude (in kilometers) and the horizontal axis is the SR value.

attenuated" or "cloudy" (to be consistent with the lidar simulator). Because, as in nature, clouds exhibit a very wide range of sizes the cloud detection is sensitive to the horizontal resolution of the data. As a test of this sensitivity, we examined the impact of resolution on the diagnosed cloud fraction by horizontally averaging the lidar signal over each 10 km prior to cloud detection. The results (not shown) indicate that the horizontal averaging can induce an artificial overestimate of the observed cloud cover in broken low-cloud cumulus fields. The overestimate ranges up to about 20–25% in the trade cumulus regime. This can be understood by considering the following idealized example: a single low-level liquid water cloud of small size (e.g., 1 km radius) surrounded by clear sky can produce locally a strong lidar backscattered signal (and thus a high SR value) which, once averaged with the surrounding clear-sky profiles, can lead to an SR value passing the cloud detection threshold (SR = 5). In such a case, a pixel of 10 km in length may thus be declared as overcast although the actual cloudiness covers only one hundredth of the area of that pixel.

[23] The GOCCP cloud detection is thus made at the full resolution of the original CALIOP level 1 data to ensure that the cloud cover is not artificially overestimated in regions where clouds have typical sizes larger than or of the order of this resolution (75 m cross track and 330 m along track below 8 km).

3.2. Sensitivity to the Vertical Grid Resolution

[24] A prerequisite for a consistent model-data comparison of the cloud fraction is that cloud layers are defined similarly in observations and in model outputs. Using lidar signals to diagnose cloud layers requires that similar SR thresholds are used for cloud detection and that these thresholds are applied at the same vertical resolution. COSP diagnostics from climate models may be analyzed either at the vertical resolution of each model (which varies from one model to another), or over a predefined vertical grid of 40 equidistant levels (the so-called COSP grid). Here, we examine the impact of vertical resolution on GOCCP cloud diagnostics.

[25] The initial CALIOP L1 data contain 583 levels with 30 m spacing between the surface and 8 km and 60 m spacing above 8 km. As shown in Figure 1, averaging CALIOP L1 data over the 40-level grid significantly

Table 2. Sensitivity to the Vertical Grid[a]

	Night		Day	
Coarse GRID	JFM	JJA	JFM	JJA
		Global		
Total	0.62	0.62	0.59	0.60
Low	0.34	0.34	0.35	0.36
Middle	0.21	0.21	0.19	0.19
High	0.16	0.16	0.16	0.16
		Land		
Total	0.48	0.46	0.47	0.49
Low	0.16	0.12	0.20	0.19
Middle	0.24	0.25	0.22	0.23
High	0.15	0.17	0.13	0.14
		Ocean		
Total	0.68	0.68	0.64	0.65
Low	0.42	0.44	0.42	0.43
Middle	0.20	0.19	0.17	0.17
High	0.16	0.16	0.16	0.16

[a]Cloud fraction diagnosed as in GOCCP but using a coarse vertical grid (19 vertical levels) instead of 40 levels.

increases the signal-to-noise ratio, and therefore minimizes the risk of false cloud detections. *Chepfer et al.* [2008] derived the CALIPSO cloud fraction for a coarser vertical grid, corresponding to the 19 vertical levels of the standard version of the LMDZ4 GCM, with 6 levels at low altitudes (below 3 km), 3 levels at middle heights (between 3 and 7.2 km), and 10 levels in the upper troposphere (above 7.2 km). In the 40-level grid, the "low-level," "middle-level" and "highest-level" atmospheric layers comprise 7, 8 and 25 levels, respectively.

[26] The total cloud cover obtained for 19 levels is about 0.05 lower than that for 40 levels (Tables 1 and 2), but this discrepancy is much more significant for the highest-level cloud fraction (up to 0.20 difference over tropical continents in the Southern Hemisphere). Likewise, we examined the effect of increasing the GOCCP data set to 80 levels at night (when signal to noise remains good at this vertical resolution) and found an increase in the cloud fraction of about 0.05. Vertical averaging lessens the contribution of optically thin cirrus clouds to the SR signal and, therefore, decreases the probability of passing the cloud detection threshold (Figure 1d). Thus, reducing the vertical resolution decreases

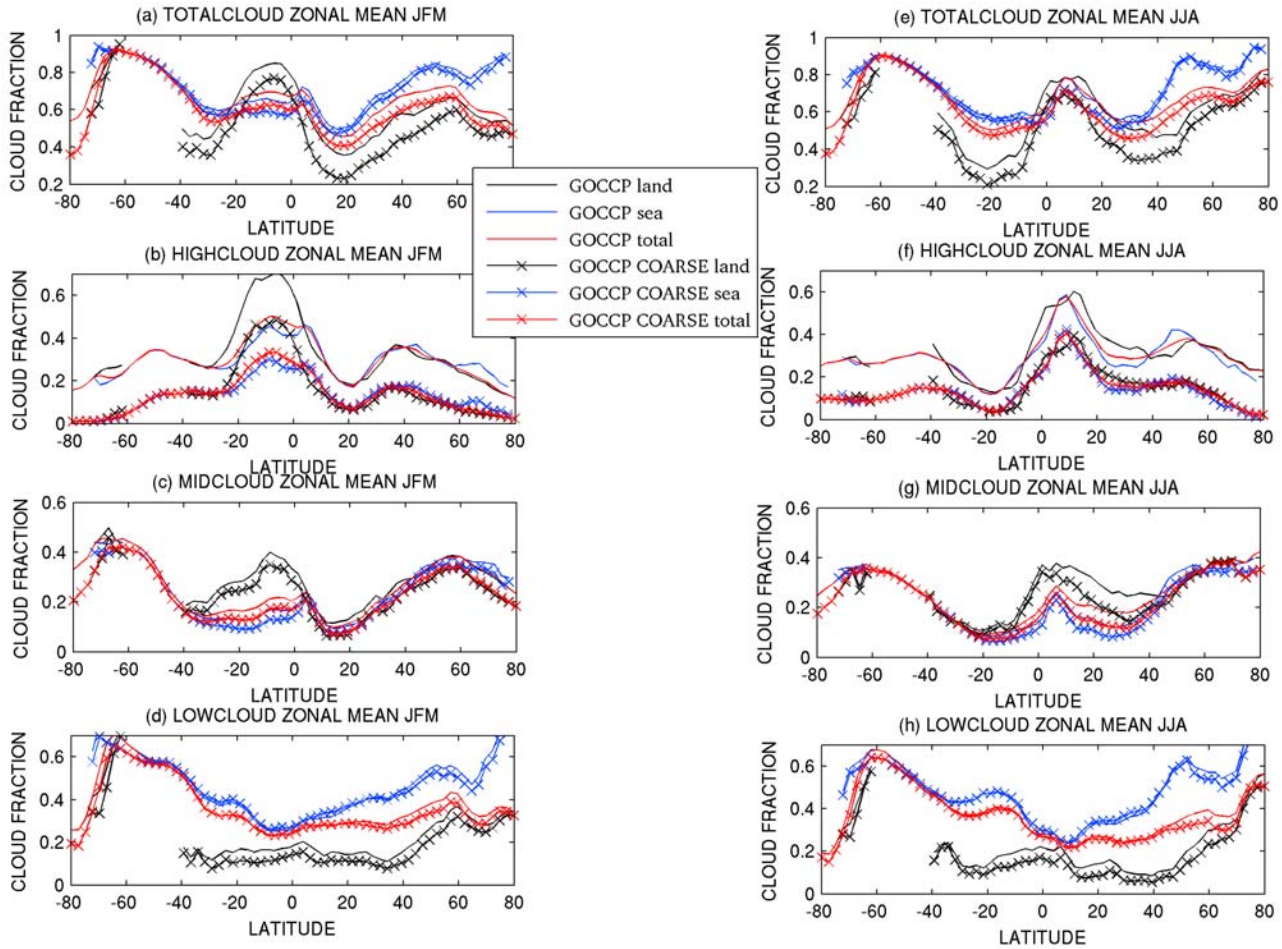

Figure 6. Sensitivity to the vertical grid day/night zonal mean (a and e) total, (b and f) highest-level, (c and g) middle-level, and (d and h) low-level cloud fraction (averaged over day and night) for JFM and JJA: above land (black), above sea (blue), and global (red). The lines without symbols are for the 40-level grid and the lines with crosses are for the coarse grid.

Table 3. Sensitivity to the Detection Threshold[a]

	GOCCP SR3	GOCCP SR5	GOCCP Coarse Grid SR3	GOCCP Coarse Grid SR5
		JJA Night		
Global				
Total	0.70	0.66	0.68	0.62
Low	0.41	0.36	0.41	0.34
Middle	0.21	0.19	0.22	0.21
High	0.29	0.29	0.16	0.16
Land				
Total	0.57	0.54	0.49	0.46
Low	0.18	0.15	0.14	0.12
Middle	0.27	0.24	0.26	0.25
High	0.31	0.31	0.17	0.17
Ocean				
Total	0.76	0.71	0.76	0.68
Low	0.51	0.45	0.53	0.44
Middle	0.18	0.17	0.20	0.19
High	0.28	0.28	0.16	0.16
		JJA Day		
Global				
Total	0.74	0.66	0.68	0.60
Low	0.46	0.37	0.46	0.36
Middle	0.33	0.25	0.21	0.19
High	0.34	0.33	0.16	0.16
Land				
Total	0.69	0.61	0.53	0.49
Low	0.33	0.25	0.24	0.19
Middle	0.40	0.31	0.26	0.23
High	0.35	0.34	0.14	0.14
Ocean				
Total	0.76	0.68	0.76	0.65
Low	0.52	0.42	0.57	0.43
Middle	0.30	0.23	0.18	0.17
High	0.34	0.33	0.17	0.16

[a]Cloud fraction diagnosed as in GOCCP but using a threshold value SR = 3 instead of SR = 5 for cloud detection.

the high-level cloud amount and, more generally, the cloud fraction associated with thin stratiform cloud layers. Figure 6 shows that this effect also impacts low- and middle-level cloud amounts with larger differences (up to 0.05) at latitudes poleward of 60°.

3.3. Sensitivity to the Cloud Detection Threshold

[27] The cloudy threshold value (here SR = 5) is a parameter of the lidar simulator that affects the detection of the optically thinner clouds. The higher the SR threshold is, the lower the cloud fraction will be and the more optically thin clouds will be missed. Typically, assuming a homogeneous boundary layer water cloud with a geometrical thickness of 250–500 m and a liquid particle radius of 12 μm, a value SR = 5 corresponds to an optical depth of 0.03–0.05 and an LWP of 0.1–0.2 g/m^2. Keeping all the others parameters constant, the optical depth will increase with the LWP and decrease when the particle size increases. On the basis of this estimate, most semitransparent clouds (optical depth >0.03) are detected, but most subvisible ones are missed. On the other hand, some very dense dust layer can be classified as cloudy when applying a simple cloud detection threshold based on SR alone. To test the sensitivity of our results to this threshold value, we computed cloud fractions for a threshold value of 3, which would detect clouds having an optical depth larger than about 0.015.

[28] When the cloud detection threshold is reduced, the mean total cloud fractions increase by about 0.05 during nighttime and by up to 0.10 during daytime (Table 3). Figure 7 shows that the total cloud cover is shifted to greater values at all latitudes except over polar regions. High-level clouds (not shown) do not contribute significantly to this increase. Subvisible clouds, that may occur, for instance, above the overshoot regions [*Dessler et al.*, 2006], are missed by both thresholds (SR = 3 and SR = 5). The total cloud cover increase is primarily driven by the global increase of the tropical low-level cloud fraction (Table 3 and Figure 7c). This latter results from a more frequent detection of optically thin and/or broken boundary layer clouds, most likely to be shallow cumulus. The middle-level cloud fraction also increases in the tropics in the area of large deserts (Figure 7b) when decreasing the cloud detection threshold, especially for daily observations (Table 3). It may be that the SR = 3 threshold detects some large smoke or dust loading events occurring in summer, and/or to the presence of thin clouds at the top of the Saharan atmospheric boundary layer.

4. Day-Night and Regional Cloud Variations

4.1. Day-Night Differences

[29] The clear-sky daytime CALIOP data are much noisier than those at night (Figure 1 versus Figure 2) because of the solar photons. About 30% of the daytime profiles are rejected after quality test on the normalization of CALIOP level 1 V2 data (section 2.1). We examine the day-night cloud cover differences to check whether the daytime data introduce a bias in the mean day/night results. The total day-night cloud cover difference is small at the global scale (<0.01, Table 1). The largest differences occur over continents where clouds are slightly more frequent during daytime at all altitudes (Table 1), but the day-night variation depends on the vertical resolution (Table 2 for the coarse grid versus Table 1 for CFMIP) and on the cloudy threshold value (SR = 3 or SR = 5, Table 3).

[30] Maps of day-night differences (Figure 8a) show that clouds are more frequent over continents during daytime (1330 LT), whereas low-level clouds are more frequent (15%) during nighttime (0130 LT) than during daytime in the tropical subsidence regions. Examination of the low, middle, and high cloud amounts independently reveals that the total day-night cloud cover variation is mostly driven by low-level clouds (Figure 8b). Both the geographical patterns and the order of magnitude of the day-night differences are in agreement with the High Resolution Infrared Sounder (HIRS) observations reported by *Wylie* [2008]. Even though, it cannot be fully asserted that the day-night variation found in GOCCP is not biased by the noise associated with solar photons (which is larger in area with bright clouds), while any bias effect is likely sufficiently small for GCM evaluation studies.

4.2. A Regional-Scale Example: Along the GPCI Transect

[31] To evaluate the cloudiness simulated by weather and climate models, the GEWEX Cloud System Study has defined a transect, named the GEWEX Pacific Cross-Section Intercomparison (GPCI) (see http://www.igidl.ul.pt/cgul/projects/gpci.htm) transect (black line in Figure 3a), that samples the stratocumulus region off the coast of California (35°N), the trade winds associated with shallow cumulus

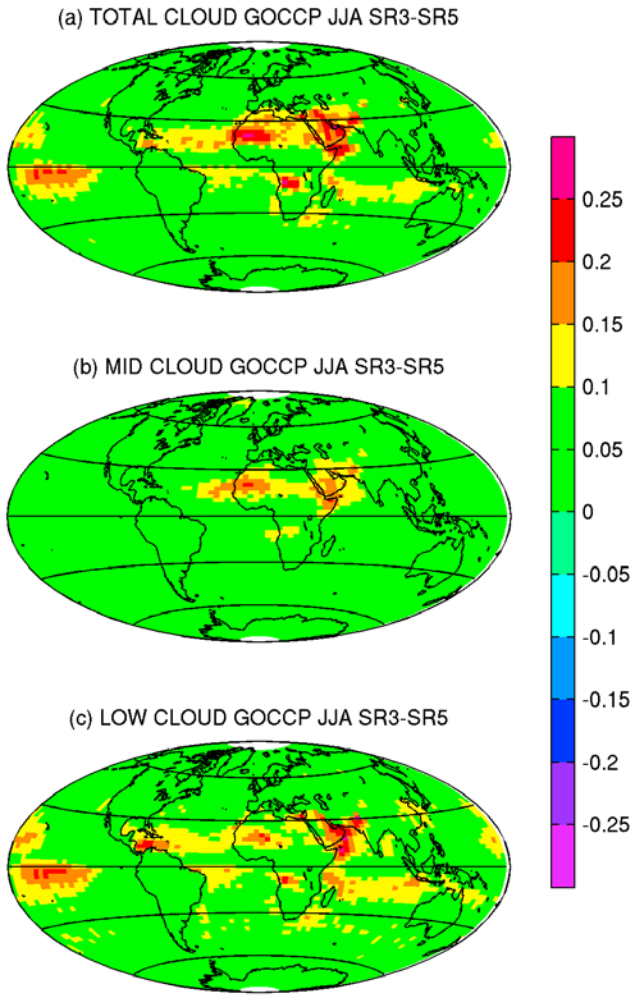

Figure 7. Difference between the cloud fractions diagnosed with a cloud detection threshold SR = 3 and SR = 5 (JJA, day/night average): (a) total, (b) middle, and (c) low cloud fraction.

clouds, and the deep convective regions of the ITCZ (0°N–12°N). The mean JJA cloud fractions along this transect are shown in Figure 9a. The stratocumulus and shallow cumulus remain below altitudes of 2400 m with most below 2000 m, and their top heights increase from 1 to 2 km away from the coast. Deep convective clouds are mostly located below 17 km, and the lidar signal is fully attenuated below 8 km (not shown), meaning that the mean cloud optical depth between 8 and 17 km is typically on the order of 3. (The optical depth of the total column can be much larger than that.) The low-level cloud fraction exceeds 0.70 (Figure 9b) along the coast and decreases southward where the middle and high cloud cover increases, masking some of the low clouds. The diagram of SR along the transect (not shown) exhibits two maxima at low altitudes: high values of SR (>60) associated with stratocumulus clouds and low values (SR < 20) corresponding to cumulus clouds.

5. Comparison With Other Cloud Climatologies

[32] The availability of satellite measurements for more than 25 years has led to several global climatologies of cloud properties. They are being intercompared within the framework of the GEWEX cloud assessment (http://climserv.ipsl.polytechnique.fr/gewexca) [*Stubenrauch et al.*, 2009].

5.1. Description of Other Cloud Climatologies

5.1.1. ISSCP

[33] The International Satellite Cloud Climatology Project (ISCCP) [*Rossow and Schiffer*, 1999] has been deriving cloud properties since 1983 using data taken by geostationary and polar orbiting weather satellites. Average ISCCP cloud amounts were computed for the period from 1984 to 2004, using 3 hourly daytime measurements from one infrared (IR) and one visible (VIS) atmospheric window channel at a spatial resolution of about 7 km, sampled every 30 km. Clouds are detected through a variable IR-VIS threshold test which compares the measured radiances to "clear-sky composite" radiances that have been inferred from a series of statistical tests on the space and time variations of the IR and VIS radiances [*Rossow and Garder*, 1993]. These clear-sky conditions are associated with low IR and VIS spatial and temporal variability.

5.1.2. TOVS Path-B and AIRS-LMD

[34] Owing to their relatively good spectral resolution, IR sounders, like the HIRS of the TIROS-N Operational Vertical Sounder (TOVS) system aboard the National Oceanic and Atmospheric Administration (NOAA) satellites or the Atmospheric Infrared Sounder (AIRS) aboard the Earth Observing Satellite (EOS) satellite Aqua, provide reliable cirrus detection, day and night. These data have been analyzed by *Stubenrauch et al.* [2006, 2008] to produce alternate long-term cloud climatologies, so far from 1987 to 1995 and from 2003 to 2008, respectively. Cloud properties have been determined at spatial resolutions of 100 km and 13 km, respectively. Whereas the TOVS Path-B cloud detection (at spatial resolution of about 17 km at nadir) is based on a combination of HIRS and Microwave Sounding Unit (MSU) measurements, the AIRS-LMD cloud retrieval, based on a weighted χ^2 method providing cloud pressure and cloud emissivity [*Stubenrauch et al.*, 1999a] (as TOVS Path-B), uses an a posteriori identification of cloudy scenes: The χ^2 method is applied to all scenes, and in a second step nonphysical results are rejected as clear or partly cloudy scenes [*Stubenrauch et al.*, 2008].

5.1.3. MODIS-CERES

[35] A shorter-term climatology of clouds is being derived from low Earth-orbiting satellites by the Clouds and the Earth's Radiant Energy System (CERES) project, which began in 1998 with the Tropical Rainfall Measuring Mission satellite, is currently operating aboard the EOS Aqua and Terra satellites, and will continue on other satellites in the future. The Aqua CERES cloud amounts and heights reported here were determined from Moderate-Resolution Imaging Spectroradiometer (MODIS) data for the period July 2002–July 2007 using the methods of *Minnis et al.* [2008a, 2008b] and *Trepte et al.* [2002]. The results are denoted as CERES-MODIS data.

5.1.4. PARASOL-PO2

[36] The PARASOL cloud products for the period January 2006 to December 2008 are derived during daytime from multispectral (visible and near infrared only) and multiangle measurements from the Polarization and Directionality of

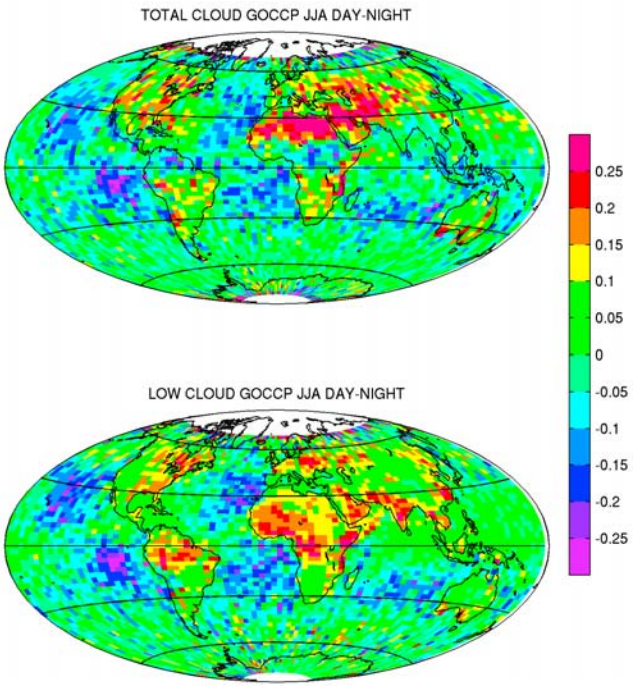

Figure 8. Cloud cover difference between daytime and nighttime GOCCP data for JJA.

the Earth Reflectances (POLDER) instrument at a native resolution of 6 km × 6 km [*Parol et al.*, 2004].

5.2. Comparison of CALIPSO-GOCCP With Other Cloud Climatologies

[37] Figure 10 presents the annually averaged global cloud cover, separately for ocean and land areas, as obtained from CALIPSO GOCCP, ISCCP, AIRS-LMD, TOVS Path-B, CERES-MODIS and POLDER3/PARASOL. For a more consistent comparison between these cloud climatologies derived from passive remote sensing and GOCCP, a version of CALIPSO GOCCP (referred to as CALIPSO-GOCCP-5 no overlap) has been treated in such a way that only the highest nonoverlapped cloud layer is taken into account. All averages are area weighted. The total cloud cover varies from 58% to 76%, depending on the sensitivity of the instrument or the retrieval algorithm or the handling of partly cloudy footprints. All climatologies show ∼10 percent more cloud cover over ocean than over land, with more low-level clouds over ocean than over land and about the same amount of high clouds over ocean and land. The cloud cover of AIRS-LMD is slightly less than that from TOVS Path-B and similar to that from ISCCP, because it corresponds to clouds for which cloud properties can be reliably determined (see above). When adding the eliminated partly cloudy footprints, weighted by a factor of 0.3, the cloud fraction rises from 0.67 to 0.75, indicating the uncertainty of cloud cover due to partly cloudy footprints. CALIOP appears to be the instrument most sensitive to cirrus, providing a high cloud cover of about 32% for CALIOP-GOCCP-5 and 40% for CALIOP-NASA, while the IR sounders provide about 30%, ISCCP about 22.5%, MODIS-CERES 20% and PARASOL only about 10%. POLDER high cloud amount is much less than that of all other climatologies due to (1) its limited ability to detect thin high clouds (no IR channels available), (2) because O_2 cloud apparent pressure is only derived over land for optical thicknesses greater than 2.0, and (3) because O_2-derived cloud apparent pressure tends to correspond to the middle of cloud pressure level [*Vanbauce et al.*, 2003]. Cirrus above low clouds are often misidentified as middle-level clouds by ISCCP [e.g., *Stubenrauch et al.*, 1999b] as well as by POLDER and CERES-MODIS. This may explain why the middle-level cloud fraction from ISCCP is larger than that of other climatologies obtained from passive remote sensing and that obtained from CALIPSO when identifying only the uppermost cloud layer (CALIPSO-GOCCP-5 no overlap).

[38] The middle-level and low-level cloud fractions from CALIPSO-GOCCP-5 are larger than that derived from ISCCP, because in addition to the uppermost cloud layers, clouds which are overlapped by higher clouds are also taken into account. The comparison of CALIPSO-GOCCP-5 with CALIPSO-GOCCP-5 no overlap shows that at a spatial resolution of 2.5° × 3.75° only about half of all low- and middle-level clouds are single layer clouds. As a consequence, low-level cloud fractions determined by AIRS-LMD, CERES-MODIS, ISCCP and TOVS Path-B fall between CALIPSO-GOCCP-SR5 and CALIPSO-GOCCP-SR5 no overlap (Figure 10). Reducing the spatial resolution will lead to a reduction of multilayer clouds: *Mace et al.* [2009] have found that 24% of all cloud systems are multilayered at a spatial resolution of 1° × 1° (requiring a 1 km gap between different cloud layers).

6. Conclusion

[39] A GCM-Oriented CALIPSO Cloud Product (GOCCP) has been developed from the CALIOP L1 data set to make consistent comparisons between CALIOP observations and "GCM + lidar simulator" outputs. For this purpose, the full horizontal resolution CALIOP level 1 data were vertically averaged at a resolution comparable to that of GCMs (40 levels), and then simple thresholds were applied to SR profiles to classify each atmospheric layer as cloudy, clear, fully attenuated or unclassified. Maps of the total cloud fraction and of the low, middle, and high layered cloud fractions, 3-D vertical distributions of the cloud fraction and joint height-SR histograms were then analyzed. The sensitivities of the results to the vertical grid and to the value of the SR threshold used for cloud detection were also studied. When decreasing the cloudy SR threshold value, the cloud fraction increases because the optically thinnest layers are better detected, independent of altitude and surface type. The effect of changing the vertical resolution (from 40 equidistant levels to 19 sigma equidistant ones) is critical for all cloud categories.

[40] The total and zonal mean cloud covers have been presented for two different seasons, JFM (January, February, and March) and JJA (June, July, and August) in accumulating 3 years of CALIOP observations (June 2006 to August 2008). The results show that large cloud fractions (>40%) are located in the marine boundary layer and that they have a significant seasonal variability; the contribution of the Southern Hemisphere tropical oceans is very significant. The seasonal variation of the global cloud cover is weak (less than 0.01), as is the globally averaged day-night

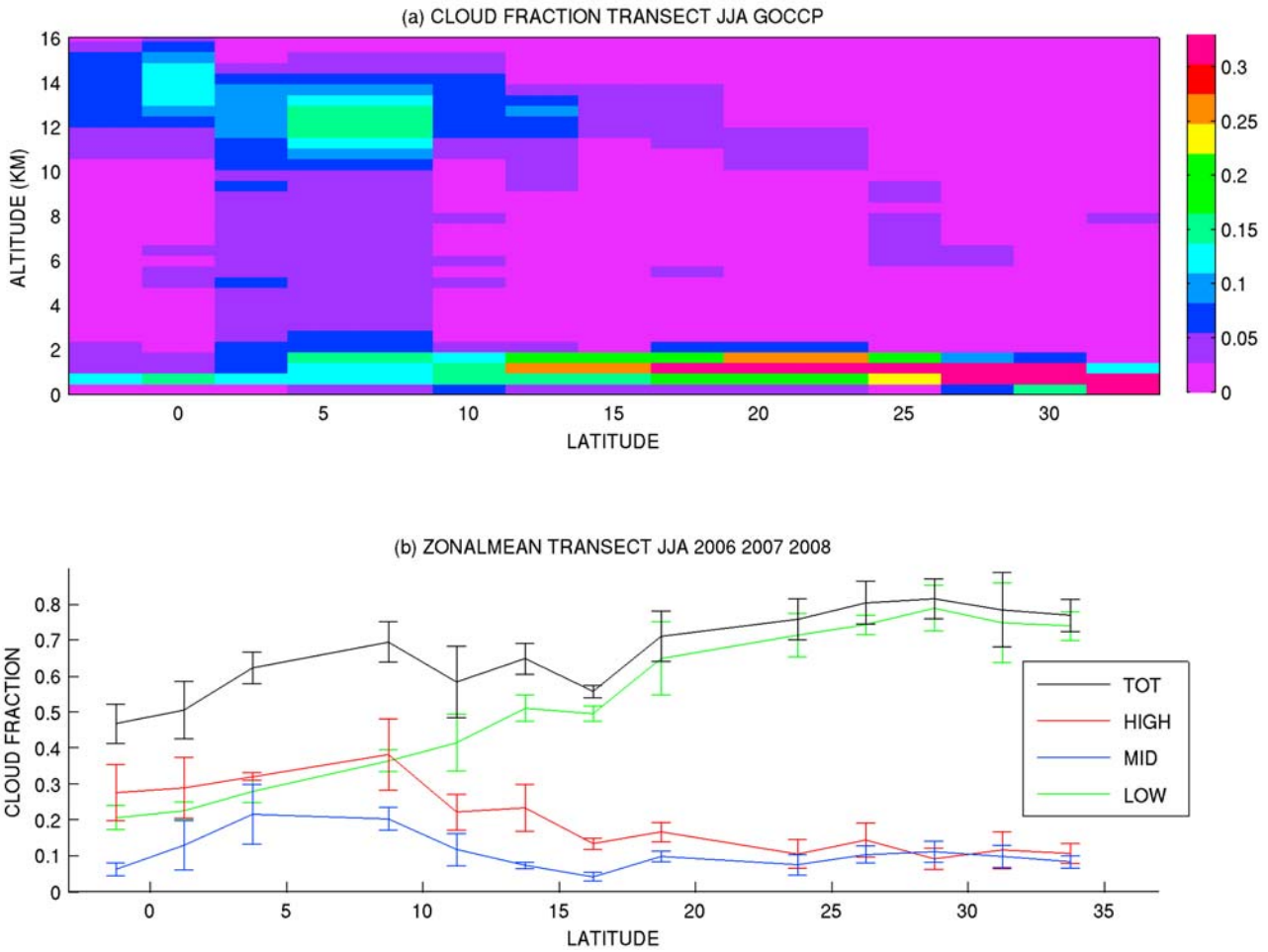

Figure 9. Cloud fraction along the GCSS Pacific Cross-Section Intercomparison (GPCI) transect (that extends over the Pacific from California to the ITCZ) in JJA: (a) vertical distribution of the cloud fraction and (b) low, middle, high, and total cloud fractions.

variation. On average, the cloud cover is greater over ocean than over land. Despite the enhanced noise of the lidar profiles in clear sky during daytime (resulting in the rejection of about 30% of the daytime profiles in this study), the day-night cloud cover difference seems robust and shows similar patterns and amplitude as the ones reported in the literature: more low-level clouds during nighttime in the oceanic subsidence regions and more clouds during daytime over land. Marine low-level clouds exhibit two categories, associated with different ranges of SR values: optically thick clouds (SR > 60) and optically thin clouds (SR < 20) that can be attributed to different horizontal cloud structure or different microphysics (particle sizes). Selected regions (tropical western Pacific, midlatitude North Pacific, and California stratocumulus) exhibit different types of SR histograms, showing the potential of such diagrams for characterizing the prominent cloud types encountered in these regions.

[41] As recommended by the WCRP Working Group for Coupled Models (http://eprints.soton.ac.uk/65383/), the COSP simulator (version v1.0) developed by CFMIP (to be made available at http://www.cfmip.net) is to be used by the climate modeling groups in some of the CMIP5 simulations (K. E. Taylor et al., unpublished manuscript, 2009,

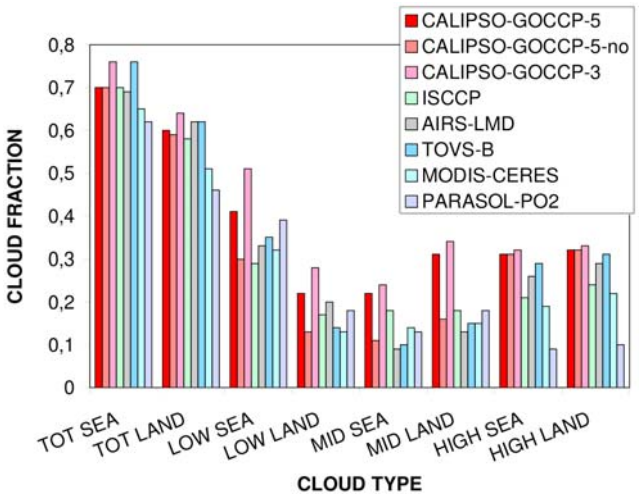

Figure 10. Comparison of GOCCP with other climatologies (annual means): O, ocean; L, land; CALIPSO-GOCCP-SR5 (06–08), same with no overlap (no cloud above); CALIPSO-GOCCP-SR3 (06–08), AIRS-LMD (03–08), ISCCP (84–04), MODIS-CERES (02–07), TOVS-B (87–95), PARASOL/POLDER (06–08).

available at http://www.clivar.org/organization/wgcm/references/Taylor_CMIP5_dec31.pdf) that will be assessed by the Fifth Assessment Report (AR5) of the Intergovernmental Panel on Climate Change (IPCC). The CALIPSO-GOCCP products presented in this article are fully consistent with the outputs from the lidar simulator used in COSP v1.0, and they are available online through the GOCCP website (http://climserv.polytechnique.fr/cfmip-atrain) at two different horizontal resolutions: $1° \times 1°$ and $2.5° \times 2.5°$. In the future, these data may thus be directly compared with the lidar simulator outputs from the CMIP5 simulations, and then be used to evaluate the cloudiness predicted by the different GCMs participating in CMIP5.

[42] **Acknowledgments.** The authors would like to thank NASA, CNES, Icare, and Climserv for giving access to the CALIOP data. This work was financially supported by CNES and by the FP6 European project ENSEMBLES. The AIRS-LMD data have been analyzed by Sylvain Cros. Thanks are due to Yan Chen and Sunny Sun-Mack (SSAI) for the CERES-MODIS data processing and to J. Riedi (LOA) for discussion and comments about POLDER3/PARASOL data. We also would like to thank the three anonymous reviewers who helped us to improve the manuscript.

References

Bey, I., D. J. Jacob, R. M. Yantosca, J. A. Logan, B. D. Field, A. M. Fiore, Q. Li, H. Y. Liu, L. J. Mickley, and M. G. Schultz (2001), Global modeling of tropospheric chemistry with assimilated meteorology: Model description and evaluation, *J. Geophys. Res.*, *106*, 23,073–23,096, doi:10.1029/2001JD000807.

Bodas-Salcedo, A., M. J. Web, M. E. Brook, M. A. Ringer, S. F. Milton, and D. R. Wilson (2008), Evaluation of cloud systems in the Met Office global forecast model using CloudSat data, *J. Geophys. Res.*, *113*, D00A13, doi:10.1029/2007JD009620.

Chepfer, H., S. Bony, D. M. Winker, M. Chiriaco, J.-L. Dufresne, and G. Seze (2008), Use of CALIPSO lidar observations to evaluate the cloudiness simulated by a climate model, *Geophys. Res. Lett.*, *35*, L15704, doi:10.1029/2008GL034207.

Dessler, A. E., S. P. Palm, W. D. Hart, and J. D. Spinhirne (2006), Tropopause-level thin cirrus coverage revealed by ICESat/Geoscience Laser Altimeter System, *J. Geophys. Res.*, *111*, D08203, doi:10.1029/2005JD006586.

Folkins, I., S. Oltmans, and A. Thompson (2000), Tropical convective outflow and near surface equivalent potential temperatures, *Geophys. Res. Lett.*, *27*, 2549–2552, doi:10.1029/2000GL011524.

Haynes, J. M., R. T. Marchand, Z. Luo, A. Bodas-Salcedo, and G. L. Stephens (2007), A multipurpose radar simulation package: QuickBeam, *Bull. Am. Meteorol. Soc.*, *88*, 1723–1727, doi:10.1175/BAMS-88-11-1723.

Johnson, R. H., T. M. Rickenback, S. A. Rutledge, P. E. Ciesielski, and W. H. Schubert (1999), Trimodal characteristics of tropical convection, *J. Clim.*, *12*, 2397–2418, doi:10.1175/1520-0442(1999)012<2397:TCOTC>2.0.CO;2.

Klein, S. A., and C. Jakob (1999), Validation and sensitivities of frontal clouds simulated by the ECMWF model, *Mon. Weather Rev.*, *127*, 2514–2531, doi:10.1175/1520-0493(1999)127<2514:VASOFC>2.0.CO;2.

Lau, N. C., and M. W. Crane (1995), A satellite view of the synoptic-scale organization of cloud properties in midlatitude and tropical circulation systems, *Mon. Weather Rev.*, *123*, 1984–2006, doi:10.1175/1520-0493(1995)123<1984:ASVOTS>2.0.CO;2.

Mace, G. G., Q. Zhang, M. Vaughan, R. Marchand, G. Stephens, C. Trepte, and D. Winker (2009), A description of hydrometeor layer occurrence statistics derived from the first year of merged Cloudsat and CALIPSO data, *J. Geophys. Res.*, *114*, D00A26, doi:10.1029/2007JD009755.

Marchand, R., J. Haynes, G. G. Mace, T. Ackerman, and G. Stephens (2009), A comparison of simulated cloud radar output from the multiscale modeling framework global climate model with CloudSat cloud radar observations, *J. Geophys. Res.*, *114*, D00A20, doi:10.1029/2008JD009790.

Minnis, P., et al. (2008a), Cloud detection in non-polar regions for CERES using TRMM VIRS and Terra and Aqua MODIS data, *IEEE Trans. Geosci. Remote Sens.*, *46*, 3857–3884, doi:10.1109/TGRS.2008.2001351.

Minnis, P., et al. (2008b), Cloud property retrievals for CERES using TRMM VIRS and Terra and Aqua MODIS data, *IEEE Trans. Geosci. Remote Sens.*, *46*, 3857–3884, doi:10.1109/TGRS.2008.2001351.

Norris, J. R., and S. F. Iacobellis (2005), North Pacific cloud feedbacks inferred from synoptic-scale dynamic and thermodynamic relationships, *J. Clim.*, *18*, 4862–4878, doi:10.1175/JCLI3558.1.

Parol, F., et al. (2004), Capabilities of multi-angle polarization cloud measurements from satellite: POLDER results, *Adv. Space Res.*, *33*, 1080–1088, doi:10.1016/S0273-1177(03)00734-8.

Rossow, W. B., and L. C. Garder (1993), Cloud detection using satellite measurements of infrared and visible radiances for ISCCP, *J. Clim.*, *6*, 2341–2369, doi:10.1175/1520-0442(1993)006<2341:CDUSMO>2.0.CO;2.

Rossow, W. B., and R. A. Schiffer (1999), Advances in understanding clouds from ISCCP, *Bull. Am. Meteorol. Soc.*, *80*, 2261–2287, doi:10.1175/1520-0477(1999)080<2261:AIUCFI>2.0.CO;2.

Sassen, K., and Z. Wang (2008), Classifying clouds around the globe with the CloudSat radar: 1-year of results, *Geophys. Res. Lett.*, *35*, L04805, doi:10.1029/2007GL032591.

Stubenrauch, C. J., A. D. Del Genio, and W. B. Rossow (1997), Implementation of sub-grid cloud vertical structure inside a GCM and its effect on the radiation budget, *J. Clim.*, *10*, 273–287, doi:10.1175/1520-0442(1997)010<0273:IOSCVS>2.0.CO;2.

Stubenrauch, C. J., A. Chédin, R. Armante, and N. A. Scott (1999a), Clouds as seen by infrared sounders (3I) and imagers (ISCCP): Part II. A new approach for cloud parameter determination in the 3I algorithms, *J. Clim.*, *12*, 2214–2223, doi:10.1175/1520-0442(1999)012<2214:CASBSS>2.0.CO;2.

Stubenrauch, C. J., W. B. Rossow, N. A. Scott, and A. Chédin (1999b), Clouds as seen by infrared sounders (3I) and imagers (ISCCP): Part III. Spatial heterogeneity and radiative effects, *J. Clim.*, *12*, 3419–3442, doi:10.1175/1520-0442(1999)012<3419:CASBSS>2.0.CO;2.

Stubenrauch, C. J., A. Chédin, G. Rädel, N. A. Scott, and S. Serrar (2006), Cloud properties and their seasonal and diurnal variability from TOVS Path-B, *J. Clim.*, *19*, 5531–5553, doi:10.1175/JCLI3929.1.

Stubenrauch, C., S. Cros, N. Lamquin, R. Armante, A. Chedin, C. Crevoisier, and N. A. Scott (2008), Cloud properties from atmospheric infrared sounder and evaluation with Cloud-Aerosol Lidar and Infrared Pathfinder Satellite observations, *J. Geophys. Res.*, *113*, D00A10, doi:10.1029/2008JD009928.

Stubenrauch, C. J., S. Kinne, and GEWEX Cloud Assessment Team (2009), Evaluation of global cloud data products, *Global Energy and Water Cycle Experiment News*, *19*(1), 6–7.

Trepte, Q., P. Minnis, and R. F. Arduini (2002), Daytime and nighttime polar cloud and snow identification using MODIS data, *Proc. SPIE*, *4891*, 449–459.

Vanbauce, C., B. Cadet, and R. T. Marchand (2003), Comparison of POLDER apparent and corrected oxygen pressure to ARM/MMCR cloud boundary pressures, *Geophys. Res. Lett.*, *30*(5), 1212, doi:10.1029/2002GL016449.

Webb, M., C. Senior, S. Bony, and J.-J. Morcrette (2001), Combining ERBE and ISCCP data to assess clouds in three climate models, *Clim. Dyn.*, *17*, 905–922, doi:10.1007/s003820100157.

Winker, D., W. Hunt, and M. McGill (2007), Initial performance assessment of CALIOP, *Geophys. Res. Lett.*, *34*, L19803, doi:10.1029/2007GL030135.

Winker, D., M. A. Vaughan, A. Omar, Y. Hu, K. A. Powell, Z. Liu, W. H. Hunt, and S. A. Young (2009), Overview of the CALIPSO mission and CALIOP data processing algorithms, *J. Atmos. Oceanic Technol.*, *26*, 2310–2323.

Wylie, D. (2008), Diurnal cycles of clouds and how they affect polar-orbiting satellite data, *J. Clim.*, *21*, 3989–3996, doi:10.1175/2007JCLI2027.1.

Yu, W., M. Doutriaux, G. Seze, H. Le Treut, and M. Desbois (1996), A methodology study of the validation of clouds in GCMs using ISCCP satellite observations, *Clim. Dyn.*, *12*, 389–401.

Zhang, M. H., et al. (2005), Comparing clouds and their seasonal variations in 10 atmospheric general circulation models with satellite measurements, *J. Geophys. Res.*, *110*, D15S02, doi:10.1029/2004JD005021.

Zhang, Y., S. Klein, G. G. Mace, and J. Boyle (2007), Cluster analysis of tropical clouds using CloudSat data, *Geophys. Res. Lett.*, *34*, L12813, doi:10.1029/2007GL029336.

S. Bony, H. Chepfer, and J. L. Dufresne, Laboratoire de Météorologie Dynamique, IPSL, Université Paris 6, Centre National de la Recherche Scientifique, Tour 45/55, 3e, 4 Place Jussieu, F-75005 Paris, France.

G. Cesana and C. J. Stubenrauch, Laboratoire de Météorologie Dynamique, IPSL, Ecole Polytechnique, Centre National de la Recherche Scientifique, F-91128 Palaiseau CEDEX, France. (chepfer@lmd.polytechnique.fr)

P. Minnis and D. Winker, NASA Langley Research Center, Mail Stop 420, Hampton, VA 23681, USA.

S. Zeng, LOA, UFR de Physique, Université des Sciences et Technologies de Lille, Bâtiment P5, F-59655 Villeneuve d'Ascq CEDEX, France.